Springer

Acta Mechanica Sinica

CrossMark click for updates

•RESEARCH PAPER•

Acta Mech. Sin., Vol. 38, 521390 (2022)
https://doi.org/10.1007/s10409-021-09031-x

Stability analysis of quasicrystal torsion micromirror actuator based on the strain gradient theory

Yunzhi Huang[1], Miaolin Feng[1*], and Xiuhua Chen[2*]

[1] *Department of Engineering Mechanics, School of Naval Architecture, Ocean and Civil Engineering, Shanghai Jiao Tong University, Shanghai 200240, China;*

[2] *School of Aeronautics and Astronautics, Shanghai Jiao Tong University, Shanghai 200240, China*

Received September 16, 2021; accepted September 24, 2021; published online February 7, 2022

Electrostatic torsional micromirrors are widely applied in the fields of micro-optical switches, optical attenuators, optical scanners, and optical displays. In previous lectures, most of the micromirrors were twisted along the uniaxial or biaxial direction, which limited the range of light reflection. In this paper, a quasicrystal torsional micromirror that can be deflected in any direction is designed and the dynamic model of the electrostatically driven micromirror is established. The static and dynamic phenomena and pull-in characteristics are analyzed through the numerical solution of the strain gradient theory. The results of three kinds of mirror deflection directions are compared and analyzed. The results show the significant differences in the torsion models with different deflection axis directions. When the deflection angle along the oblique axis reaches 45°, the instability voltage is the smallest. The pull-in instability voltage increases with the increment of phonon-phason coupling elastic modulus and phason elastic modulus. The permittivity of quasicrystal, the strain gradient parameter, and the air damping influence the torsion of the micromirror dynamic system. A larger pull-in instability voltage generates with the decrease of surface distributed forces.

Quasicrystals, Torsion micromirror, Instability, Strain gradient theory

Citation: Y. Z. Huang, M. L. Feng, and X. H. Chen, Stability analysis of quasicrystal torsion micromirror actuator based on the strain gradient theory, Acta Mech. Sin. **38**, 521390 (2022), https://doi.org/10.1007/s10409-021-09031-x

1. Introduction

Microelectromechanical system (MEMS) is an independent intelligent system, its internal structure is generally in micron or even nanometer scale. With the rapid development of micromachining technology, optical devices based on micro/nanoelectromechanical systems (M/NEMS) with complex functions and excellent performance have been widely used in the fields of micro-nano optical switch, optical attenuator, optical scanner, and optical display, which is called micro/nano-opto-electromechanical system (M/NOEMS) [1]. The electrostatic driving micromirror actuator is mainly divided into two types: planar micromirror actuator and torsional micromirror actuator. Planar micromirror actuator adopts micromirror translation mode, but the driving time is relatively long, and the surface roughness problem will be caused by silicon etching process; therefore, the torsion micromirror driver is more commonly used in micro/nano functional devices, which uses electrostatic torsion micromirror main plate movement, and realizes the driver function through the rotation angle of micromirror main plate and the torque of micro/nanobeam connected and supported at both ends [2,3]. Electrostatically driven MEMS torsional micromirrors are widely used in various fields. Like all microdevices driven by electrostatic force, the pull-in instability phenomenon may happen in the MEMS torsional micromirrors [4]. At first, the pull-in analysis developed from the perspective of static balance. For example, early researchers carried out theoretical analysis and experimental verification on the static characteristics of micromirrors, which showed that the

*Corresponding authors. E-mail addresses: mlfeng@sjtu.edu.cn (M. L. Feng); chenxiuhua@sjtu.edu.cn (X. H. Chen)
Executive Editor: Yanqing Wang

relationship between pull-in angle and electrode size [5]. Recently, the more precise motion controls on MEMS micromirrors were studied. To reduce the driving voltage, Sadhukhan et al. [6] replaced the straight torsion springs with comb structures that connect the mirror to the gimbal in the two-axis tilt scanning micromirror. Hua et al. [7] considered the external vibration in the motion control of MEMS micromirrors and proposed a feedforward sliding mode control method.

In the study of micromirror dynamics, people realize that the pull-in of the micromirror system is related to the typical saddle-node bifurcation instability of a nonlinear system [8]. Therefore, on the one hand, researchers solve the static equilibrium equation of micromirror and directly solve the dynamic differential equation in the time domain to study the pull-in instability of micromirror [9]. On the other hand, through the state space analysis method, the bifurcation phenomenon of the micromirror nonlinear system is studied, to capture the sudden change of the global behavior of the system, and deeply understand the stability and pull-in of the system [10]. Although the unidirectional and bidirectional of the electrostatically driven micromirror system have been studied by the state space and dynamic analysis method [11], the torsion direction of the micromirror model is relatively simple.

Generally, nanomaterials and structures exhibit significant lateral dependence, which is different from the case at the macroscale. Therefore, several key theories consider nanoscale characteristics. One classical theory was the nonlocal elasticity theory that was applied to investigate the size-dependent instability of carbon nanotubes under electrostatic actuation [12]. In the sense of nonlocal interaction, a nonlocal operator method for the solution of partial differential equations [13] and boundary value problems [14] was proposed by Ren et al. The final discrete equation can be obtained based on the functional of the nonlocal operator, which has great advantages in solving higher-order partial differential equations. Besides, the coupled stress theory [15], the strain gradient elastic theory [16], and the surface effect [17] have also been successively proposed to better explain the pull instability of nanoscale actuators. In this paper, the theory of strain gradient is introduced to characterize the size effect of nano-actuators. Because the strain gradient parameter has a strengthening effect on the stiffness of the nanobeam in the model, the influence of the relationship between the torsion angle and the plate spacing on the pull-in instability of the electrostatically driven torsion micromirror is studied in the framework of the modified strain gradient theory. In addition to two classical elastic parameters, the modified strain gradient theory also includes three independent intrinsic length parameters to reflect the size dependence of micro/nanostructures [18-23].

Recently, quasicrystals (QCs) reinforced composites have attracted enormous interest from researchers since QCs as promising reinforcement have excellent electro-mechanical and physical behaviors with low density [24]. Furthermore, conductivity, lightweight, low fabrication cost, and fine stretch ability enable QCs to have great potential in the application of nano-electromechanical devices [25]. Fournée et al. [26] studied metal films grown on QC substrates and concluded that quantum size effects are common on quasicrystalline substrates. Inoue et al. [27] found that the hardness, Young's modulus, fatigue strength, and tensile strength of Al-based nanocrystalline alloys were higher than those of traditional Al-based alloys. Moreover, based on the nonlocal strain gradient theory, Zhang et al. [28] studied the static bending deformation of a functionally graded multilayered nanoplate made of piezoelectric QC materials. Li et al. [29] analyzed the static bending deformation of multilayered QC nanoplates under surface loadings using the modified couple stress theory. With the increasing development of nanofabrication techniques, more and more QCs based M/NEMS devices will be fabricated and ameliorated for meeting future versatile demands. Therefore, it is significant to investigate the pull-in instability of QC torsional micromirror considering scale and surface effects further.

This paper will explore the pull-in instability of a multi-directional QC torsion micromirror actuator. Firstly, the static and dynamic model of the torsional micromirror system with a QC circular main plate is established based on the modified strain gradient theory. The relationship between the torsional angle, the torsion direction, and the pull-in instability voltage of the micromirror is discussed. The effects of QC material parameters and geometric parameters on the pull-in instability are given. Secondly, the influence of the strain gradient parameter-induced additional stiffness and air damping on the pull-in instability is studied. Finally, the effects of van der Waals moment and thermal Casimir moment on the pull-in instability voltage are revealed.

2. Basic equations

To study the influence of the relative relationship between torsion angle and plate spacing based on the modified strain gradient theory on the nonlinear coupling effect of forces, while verifying the main plate of micromirror with the rectangular electrostatic field in the literature, the structure of the main plate is extended to circular. Figure 1 shows the main view and details of the whole mirror system. The outer ring rotates the whole circular plate structure around the horizontal axis or other axes under the electrostatic force from the base electrode in Fig. 1a. The two inner springs along the vertical axis connect the inner round plate to the outer combination of beams. The two outer springs along the vertical axis connect the outer beam to the fixed support. In the top view of the circular plate (Fig. 1b), the radius of the circular plate is R. The inner and outer lengths of the beams

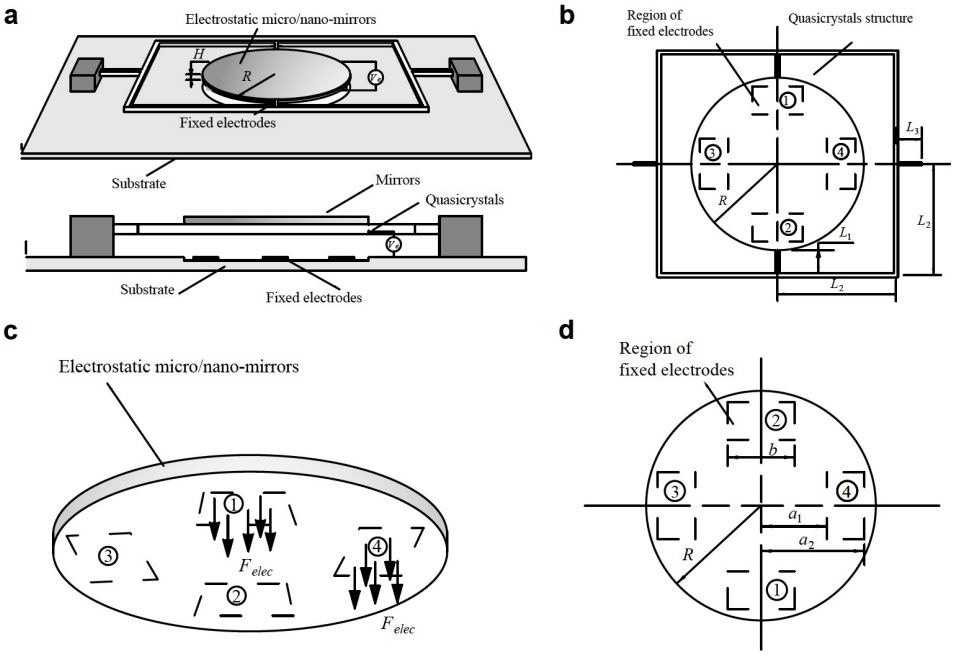

Figure 1 A schematic view of the round, double-gimbaled system, showing the various relevant parameters: **a** the main view of the system; **b** the top view of the circular plate; **c** the bottom view of the circular plate; **d** the top view of the substrate.

are L_1 and L_2, respectively. The distance from the fixed support to the square frame of the beam is L_3. The bottom view of the circular plate is shown in Fig. 1c. In the top view of the substrate (Fig. 1d), the distance from the center of the plate to the head and end of rectangle electrodes are a_1 and a_2. The width of the rectangle electrode is b. The structure thickness is H. The width and thickness of each spring beam are h_1 and h_2 respectively. In this paper, the spring height equals H. The angle between the circular plate and the fixed electrode plane is θ. Figure 2 displays the torsional micromirror model considering the effect of torsion bending coupling deformation. The initial gap between the circular plate and the substrate is g_0 and the deformation of the plate is δ. The structure is connected with external voltage V_e.

Applying the voltage between the main plate and electrode

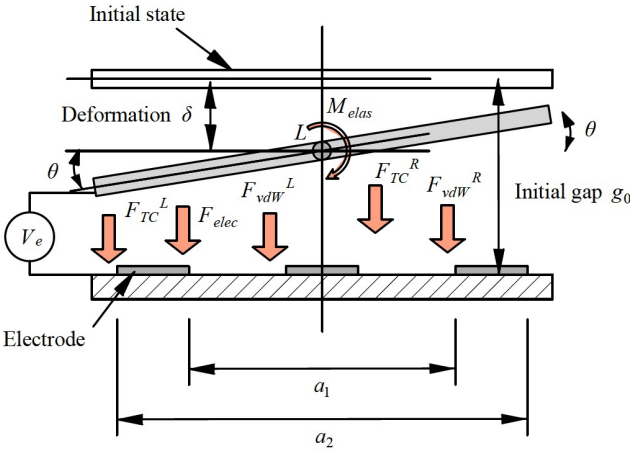

Figure 2 Schematic diagram of electrostatic torsional mirror with model considering coupled torsion and bending effects.

creates the attraction between them and causes the plate to turn toward the electrode based on Coulomb's law. To develop the governing equations of the problem, vertical displacements of the plate and axial displacements of the torsional beam are assumed to be infinitesimal so that the pull-in instability occurs. It is acceptable for this assumption to create an error of lower than 1% in the investigation of MEMS [30]. The ratio of circular plate thickness to the radius and the ratio of elastic displacement to the torsional amplitude are so small that the angle θ can be used as the angle between the circular plate and the fixed electrode plane [11]. For this model, it is possible that in torsional MEMS in absence of applied voltage pull-in instability still occurs owing to the existence of intermolecular forces such as the Casimir force. So the amount of gap between the main plate and the underside electrode is significant for prevention from pull-in. Meanwhile, the electric field distribution needs to be standardized on the electrical substrate. The value of the applied voltage should also be accurately controlled to achieve pull-in instability.

For the electrostatically driven torsion micromirror with a QC main plate, the electric field force acting on the differential element on the main plate can be obtained by the following relation [11,31]:

$$\mathrm{d}F_{\mathrm{elec}} = \frac{(\varepsilon_0+\varepsilon_1)V_e^2 b}{2(g_0-\delta-r\sin\theta)^2}\mathrm{d}r, \tag{1}$$

where $\varepsilon_0 = 8.854 \times 10^{-12}\ \mathrm{C^2/(N\,m^2)}$ is the permittivity of vacuum and ε_1 is the permittivity in the phason field from the epilayer of QC surface [31], δ is the displacement of the main plate of the micromirror, r is the radial component of a cir-

cular main plate in polar coordinates. At the same time, the electric field moment of the differential unit on the main plate of the micromirror can be obtained by the following relation:

$$\mathrm{d}M_{\mathrm{elec}} = \frac{(\varepsilon_0+\varepsilon_1)V_{\mathrm{e}}^2 b}{2(g_0-\delta-r\sin\theta)^2} r\mathrm{d}r. \tag{2}$$

The total electric field force acting on the main plate of the micromirror can be obtained by integrating the elements:

$$\begin{aligned} F_{\mathrm{elec}} &= \int_{a_1/2}^{a_2/2} \mathrm{d}F_{\mathrm{elec}} \\ &= \frac{(\varepsilon_0+\varepsilon_1)V_{\mathrm{e}}^2 b}{2\sin\theta}\left(\frac{1}{g_0-\delta-\frac{a_2}{2}\sin\theta}-\frac{1}{g_0-\delta-\frac{a_1}{2}\sin\theta}\right). \end{aligned} \tag{3}$$

Then the total electrostatic driving moment of the micromirror main plate about the rotation axis can be obtained by integrating the whole main plate:

$$\begin{aligned} M_{\mathrm{elec}} &= \int_{a_1/2}^{a_2/2} \mathrm{d}M_{\mathrm{elec}} \\ &= \frac{(\varepsilon_0+\varepsilon_1)V_{\mathrm{e}}^2 b}{2\sin\theta}\left[\frac{1}{g_0-\delta-\frac{a_2}{2}\sin\theta}-\frac{1}{g_0-\delta-\frac{a_1}{2}\sin\theta}\right. \\ &\quad \left.+\ln\left(\frac{g_0-\delta-\frac{a_2}{2}\sin\theta}{g_0-\delta-\frac{a_1}{2}\sin\theta}\right)\right]. \end{aligned} \tag{4}$$

When the direction of electric field moment is counterclockwise rotation along the middle L axis, the plate rotates counterclockwise in Fig. 2. Considering that the micromirror has a small torsion angle $\theta < 5°$ and $\sin\theta \approx \theta$, the total electric field force acting on the main plate of the micromirror and the moment caused by the electric field force can be further simplified:

$$F_{\mathrm{elec}} = \frac{(\varepsilon_0+\varepsilon_1)V_{\mathrm{e}}^2 b}{2\theta}\left(\frac{1}{g_0-\delta-\frac{a_2}{2}\theta}-\frac{1}{g_0-\delta-\frac{a_1}{2}\theta}\right), \tag{5}$$

$$\begin{aligned} M_{\mathrm{elec}} &= \frac{(\varepsilon_0+\varepsilon_1)V_{\mathrm{e}}^2 b}{2\theta}\left[\frac{1}{g_0-\delta-\frac{a_2}{2}\theta}-\frac{1}{g_0-\delta-\frac{a_1}{2}\theta}\right. \\ &\quad \left.+\ln\left(\frac{g_0-\delta-\frac{a_2}{2}\theta}{g_0-\delta-\frac{a_1}{2}\theta}\right)\right]. \end{aligned} \tag{6}$$

Considering the moment to the micromirror main plate caused by thermal fluctuation Casimir force, based on the Plasma theoretical model [30,32], the expressions of thermal fluctuation Casimir force on the unit area of the left and right sides of the micromirror circular main plate can be obtained respectively, i.e.,

$$\begin{aligned} \mathrm{d}F_{CT}^{\mathrm{L}} &= \left\{\frac{\pi^2\hbar c_0}{240(g_0-\delta-r\sin\theta\sin\varphi)^4}\left[1+\frac{1}{3}\left(\frac{2(g_0-\delta-r\sin\theta\sin\varphi)k_{\mathrm{B}}T}{\hbar c_0}\right)^4\right]+\frac{k_{\mathrm{B}}T\zeta(3)}{4\pi^2(g_0-\delta-r\sin\theta\sin\varphi)^3}\right\} r\mathrm{d}r\mathrm{d}\varphi, \\ \mathrm{d}F_{CT}^{\mathrm{R}} &= \left\{\frac{\pi^2\hbar c_0}{240(g_0-\delta+r\sin\theta\sin\varphi)^4}\left[1+\frac{1}{3}\left(\frac{2(g_0-\delta+r\sin\theta\sin\varphi)k_{\mathrm{B}}T}{\hbar c_0}\right)^4\right]+\frac{k_{\mathrm{B}}T\zeta(3)}{4\pi^2(g_0-\delta+r\sin\theta\sin\varphi)^3}\right\} r\mathrm{d}r\mathrm{d}\varphi, \end{aligned} \tag{7}$$

where φ represents the circumferential component of a circular main plate in polar coordinates, $\hbar = 1.055 \times 10^{-34}$ Js is the Plank's constant divided by 2π and $c_0 = 3.0 \times 10^8$ m/s is the speed of light. $k_{\mathrm{B}} = 1.38 \times 10^{-23}$ is the Boltzmann constant, T is the thermal environment temperature and $\zeta(3) = 1.212$ is the Riemann zeta function. It should be pointed out that when $T \to 0$, Eq. (7) degenerates to the expression of quantum wave Casimir force without considering the influence of finite temperature. Therefore, the moment caused by thermal fluctuation Casimir force per unit area can be expressed as:

$$\begin{aligned} \mathrm{d}M_{CT}^{\mathrm{L}} &= \left\{\frac{\pi^2\hbar c_0}{240(g_0-\delta-r\sin\theta\sin\varphi)^4}\left[1+\frac{1}{3}\left(\frac{2(g_0-\delta-r\sin\theta\sin\varphi)k_{\mathrm{B}}T}{\hbar c_0}\right)^4\right]+\frac{k_{\mathrm{B}}T\zeta(3)}{4\pi^2(g_0-\delta-r\sin\theta\sin\varphi)^3}\right\} r^2\cos\theta\sin\varphi\mathrm{d}r\mathrm{d}\varphi, \\ \mathrm{d}M_{CT}^{\mathrm{R}} &= \left\{\frac{\pi^2\hbar c_0}{240(g_0-\delta+r\sin\theta\sin\varphi)^4}\left[1+\frac{1}{3}\left(\frac{2(g_0-\delta+r\sin\theta\sin\varphi)k_{\mathrm{B}}T}{\hbar c_0}\right)^4\right]+\frac{k_{\mathrm{B}}T\zeta(3)}{4\pi^2(g_0-\delta+r\sin\theta\sin\varphi)^3}\right\} r^2\cos\theta\sin\varphi\mathrm{d}r\mathrm{d}\varphi. \end{aligned} \tag{8}$$

Furthermore, the resultant moment caused by thermal Casimir force can be obtained by integrating the semicircular areas of the two sides of the main plate:

$$M_{CT}=\int_0^{\pi}\int_0^{R}\left\{\frac{\pi^2\hbar c_0}{240(g_0-\delta-r\sin\theta\sin\varphi)^4}\left[1+\frac{1}{3}\left(\frac{2(g_0-\delta-r\sin\theta\sin\varphi)k_BT}{\hbar c_0}\right)^4\right]+\frac{k_BT\zeta(3)}{4\pi^2(g_0-\delta-r\sin\theta\sin\varphi)^3}\right\}$$
$$\cdot r^2\cos\theta\sin\varphi\mathrm{d}r\mathrm{d}\varphi-\int_0^{\pi}\int_0^{R}\left\{\frac{\pi^2\hbar c_0}{240(g_0-\delta+r\sin\theta\sin\varphi)^4}\left[1+\frac{1}{3}\left(\frac{2(g_0-\delta+r\sin\theta\sin\varphi)k_BT}{\hbar c_0}\right)^4\right]\right.$$
$$\left.+\frac{k_BT\zeta(3)}{4\pi^2(g_0-\delta+r\sin\theta\sin\varphi)^3}\right\}r^2\cos\theta\sin\varphi\mathrm{d}r\mathrm{d}\varphi. \tag{9}$$

The left and right Casimir moments ($\mathrm{d}M_{CT}^{\mathrm{L}}$ and $\mathrm{d}M_{CT}^{\mathrm{R}}$) rotate counterclockwise and clockwise along the middle L axis in Fig. 2, respectively. The resultant moment of the two rotates counterclockwise along the middle L axis because the Casimir force is negatively correlated with the spacing between the two interfaces, as shown in Eq. (9). Then, the symbolic definite integral of Eq. (9) is calculated and the corresponding mathematical simplification is carried out:

$$M_{\mathrm{CT}}=\frac{\pi^3\hbar c_0R^4\theta}{240[(g_0-\delta)^2-R^2\theta^2]^{5/2}}+\frac{60k_BT\zeta(3)}{240\pi\theta^3}$$
$$\cdot\left[-\frac{2(g_0-\delta)}{\sqrt{(g_0-\delta)^2-R^2\theta^2}}+\frac{(g_0-\delta)R^2\theta^2}{[(g_0-\delta)^2-R^2\theta^2]^{3/2}}+2\right]. \tag{10}$$

The expression of van der Waals force on the unit area of the left and right sides of the circular main plate of the micromirror are

$$\mathrm{d}F_{\mathrm{vdW}}^{\mathrm{L}}=\frac{\overline{A}}{6\pi(g_0-\delta-r\sin\theta\sin\varphi)^3}r\mathrm{d}r\mathrm{d}\varphi,$$
$$\mathrm{d}F_{\mathrm{vdW}}^{\mathrm{R}}=\frac{\overline{A}}{6\pi(g_0-\delta+r\sin\theta\sin\varphi)^3}r\mathrm{d}r\mathrm{d}\varphi, \tag{11}$$

where $\overline{A}=15.2\times10^{-20}$ is the Hamaker constant. The rotation moment of the micromirror main plate caused by van der Waals force per unit area can be expressed as:

$$\mathrm{d}M_{\mathrm{vdW}}^{\mathrm{L}}=\frac{\overline{A}}{6\pi(g_0-\delta-r\sin\theta\sin\varphi)^3}r^2\cos\theta\sin\varphi\mathrm{d}r\mathrm{d}\varphi,$$
$$\mathrm{d}M_{\mathrm{vdW}}^{\mathrm{R}}=\frac{\overline{A}}{6\pi(g_0-\delta+r\sin\theta\sin\varphi)^3}r^2\cos\theta\sin\varphi\mathrm{d}r\mathrm{d}\varphi. \tag{12}$$

Then the resultant van der Waals moment acting on the main plate of the micromirror can be obtained by integrating the area of the circular main plate and making corresponding mathematical simplification:

$$M_{\mathrm{vdW}}=\frac{\overline{A}}{12}\left[\frac{2(g_0-\delta-R^2\theta^2)^{3/2}+3(g_0-\delta)R^2\theta^2-2(g_0-\delta)^3}{\theta^3\left[(g_0-\delta)^2-R^2\theta^2\right]^{3/2}}\right]. \tag{13}$$

Similar to the resultant Casimir moment, the resultant van der Waals moment of the two rotates counterclockwise along the middle L axis in Fig. 2. For the micro/nano electronic devices that cannot be vacuum packaged, the devices work under different environmental pressures. If there is a thin layer of air between the micromirror main plate and the fixed electrode, the squeeze film damping effect will be produced due to the movement of the micromirror main plate and the extrusion of the middle air layer [33,34]. According to the Reynolds equation, the expression of the film damping force on the left and right half of the unit area of the circular main plate is [35]

$$\frac{\mathrm{d}F_{\mathrm{sq}}^{\mathrm{L}}\mathrm{d}t}{\mathrm{d}u}=-\frac{C_{\mathrm{d}}}{(g_0-\delta-r\sin\theta\sin\varphi)^3}r\mathrm{d}r\mathrm{d}\varphi,$$
$$\frac{\mathrm{d}F_{\mathrm{sq}}^{\mathrm{R}}\mathrm{d}t}{\mathrm{d}u}=-\frac{C_d}{(g_0-\delta+r\sin\theta\sin\varphi)^3}r\mathrm{d}r\mathrm{d}\varphi, \tag{14}$$

where t represents the time of model motion and $u=R\cdot\theta$. For the rigid rotating micromirror main plate, the film damping coefficient C_{d} can be determined by the moment and torsional angle speed caused by the film damping force on the circular main plate.

The expression (14) of the film damping coefficient is treated by the approximate relationship of the small torsion angle of the micromirror main plate, and the first three terms are expanded by the Taylor series to obtain the simplified analytical expression of the film damping coefficient, that is

$$C_{\mathrm{sq}}=C_{\mathrm{d}}\frac{R^3}{{g_0}^3}\left(\frac{4}{3}+\frac{16}{5}\frac{R^2\theta^2}{{g_0}^2}+\frac{32}{7}\frac{R^4\theta^4}{{g_0}^4}+\ldots\right). \tag{15}$$

3. Analytical solutions

The electrostatic, van der Waals, and Casimir forces as the distributed forces on the bottom surface of the circular plate are considered. For an electrostatically driven micromirror system with a circular main plate, the equilibrium equation of rigid rotation under the combined action of film damping, electrostatic, van der Waals, and Casimir moments, and elastic torques become:

$$I_q\frac{\partial^2\theta}{\partial t^2}+(C_{\rm vq}+C_{\rm sq})\frac{\partial\theta}{\partial t}+2M_{\rm elas1}+4M_{\rm elas2}-M_{\rm elec}-(1-n)\cdot M_{\rm vdW}-n\cdot M_{\rm CT}=0, \tag{16}$$

where, $I_{\rm q}$ is the moment of inertia of the micromirror circular main plate rotating around the central axis, and $I_{\rm q}=\pi R^4/4$. $C_{\rm vq}$ and $C_{\rm sq}$ are the structural damping coefficient and the pressed film damping coefficient respectively. It is a static behavior when the applied voltage is below the pull-in value, while the instability of the micromirror happens after breaking through this value.

Due to the strengthening effect of strain gradient parameter on the stiffness of micron beam, the influence relationship between torsional angle and plate spacing on the pull-in instability of electrostatically driven torsional micromirror is considered based on the modified strain gradient theory. According to the modified strain gradient theory [20] and the strain gradient warpage function [36] in the literatures, the total torques causing the torsional deformation of the rectangular section nanobeam can be expressed in the following form:

$$\begin{aligned}M_{\rm elas1}&=\frac{G}{L_1}(J_0+J_{\rm S})\theta,\\ M_{\rm elas2}&=\frac{G}{L_2}(J_0+J_{\rm S})\frac{\theta}{2},\end{aligned} \tag{17}$$

where J_0 is the polar moment of inertia of the nanobeam rotation, $J_{\rm S}$ is the additional polar moment of inertia with the size effect caused by the strain gradient parameter. For micron beams with the rectangular section, the following relationship is satisfied:

$$J_{{\rm S}i}=3AL_i^2+\iint_A\left(x\frac{\partial\psi}{\partial y}-y\frac{\partial\psi}{\partial x}\right){\rm d}A, \tag{18}$$

where A is the cross-sectional area of the beam, x and y are the two coordinate axes in the horizontal direction with the origin at the center of the plate circle, and ψ is the strain function. It should be noted that the additional polar moment of inertia $J_{\rm S}$ includes the Saint Venant torsion function reflecting the cross-section warpage and the intrinsic length parameter reflecting the size dependence [36]. The shear modulus is expressed as:

$$G=\frac{E}{2(1+\nu)}=\frac{iE_c+jR_1+kK_1}{2(1+\nu)}, \tag{19}$$

is the shear modulus of the beam [25]. The elastic moduli E includes phonon elastic moduli E_c, the phason elastic moduli K_1, and the phonon-phason coupling elastic modulus R_1. The sum of the three coefficients i, j, and k is 1. The directions of moments for squeeze film damping and the torque for torsional deformation are clockwise along the middle L axis.

Before the pull-in instability, the micromirror system is in equilibrium under the combined action of internal elastic strain torques, external film damping moment, and moments caused by micro distributed force. Therefore, the equilibrium equation is given

$$I_q\frac{\partial^2\theta}{\partial t^2}+(C_{\rm vq}+C_{\rm sq})\frac{\partial\theta}{\partial t}+2M_{\rm elas1}+4M_{\rm elas2}-M_{\rm elec}-(1-n)\cdot M_{\rm vdW}-n\cdot M_{CT}=0. \tag{20}$$

When $n=0$, the van der Waals force is considered; when $n=1$, thermal Casimir force is considered in the micromirror system, which depends on the size range of plate spacing in the actual design. For the circular main plate micromirror system, Eqs. (6), (10), (13), (14), and (17) are substituted into Eq. (20) to obtain the dimensionless equilibrium equation of the micromirror system considering the micro distributed force, that is

$$\begin{aligned}&\frac{\partial^2\Theta}{\partial\tau^2}+\left[\overline{C}_{vq}+\overline{C}_{sq}\left(\frac{4}{3}+\frac{16}{5}\Theta^2+\frac{32}{7}\Theta^4\right)\right]\frac{\partial\Theta}{\partial\tau}+2GJ_0\left(1+\frac{J_S}{J_0}\right)\frac{g_0(L_1+L_2)}{aL_1L_2}\Theta-\frac{(\varepsilon_0+\varepsilon_1)V_e^2ba^2}{2g_0^2}\frac{1}{\Theta^2}\cdot\\ &\left[\frac{1-\Delta_1}{1-\Delta_1-\lambda_2\cdot\Theta}-\frac{1-\Delta_1}{1-\Delta_1-\lambda_1\cdot\Theta}+\ln\left(\frac{1-\Delta_1-\lambda_2\cdot\Theta}{1-\Delta_1-\lambda_1\cdot\Theta}\right)\right]-(1-n)\alpha_{3tt}\left[\frac{2(1-\Delta_1-\Theta^2)^{3/2}+3\Theta^2-2}{(1-\Delta_1-\Theta^2)^{3/2}}\right]\\ &-\frac{n\alpha_{4tt}\Theta}{\left(1-\Delta_1-\Theta^2\right)^{5/2}}-\frac{n\alpha_{5tt}}{\Theta^3}\left[-\frac{2}{(1-\Delta_1-\Theta)^{1/2}}+\frac{\Theta^2}{(1-\Delta_1+\Theta)^{3/2}}+2\right]=0,\end{aligned} \tag{21}$$

where the corresponding dimensionless variables are defined as follows:

$$J_{\mathrm{R}}=\frac{J_{\mathrm{S}}}{J_0},\quad d=\frac{g_0}{R},\quad \Theta=\frac{\theta}{d},$$
$$\beta_{tt}=V_{\mathrm{e}}\sqrt{\frac{(\varepsilon_0+\varepsilon_1)Lg_0}{4GJ_0d^4}},$$
$$\tau=t\sqrt{\frac{2G}{L_1}},\ \alpha_{3tt}=\frac{\alpha_3\overline{A}R^4L}{24g_0^4GJ_0},\tag{22}$$
$$\alpha_{4tt}=\frac{\alpha_4\pi^3\hbar c_0R^4L}{480g_0^5GJ_0},$$
$$\alpha_{5tt}=\frac{60\alpha_4k_{\mathrm{B}}T\zeta(3)R^4L}{480\pi g_0^4GJ_0},$$

where d and Θ denote the dimensionless plate spacing and torsion angle respectively, $\overline{C}_{\mathrm{vq}}$ and $\overline{C}_{\mathrm{sq}}$ are the dimensionless structural damping coefficient and the pressed film damping coefficient respectively. Because the plate spacing is far less than the radius of the circular main plate, that is, $g_0/R << 1$, the variation range of the torsion angle is very small. The dimensionless maximum torsion angle satisfies the relation $\Theta_{\max}= d$. The physical meaning of the dimensionless plate spacing d is the ratio of the spacing between the torsion micromirror main plate and the bottom fixed plate to the radius of the circular main plate. $\Delta_1 = \delta / R$ is the static displacement for the bending deformation under electrostatic force, and it can be solved by removing the time and torsion terms from the governing equation.

The applied voltage V_{e} can be expressed from Eq. (21). When the applied voltage increases, the torsion angle of the micromirror main plate increases, and the side of the micromirror main plate first tends to be close to the bottom fixed plate; the design problem caused by this phenomenon is that the distance between the main plate and the fixed plate of the micromirror needs to be set reasonably in order to avoid the pull-in instability within the allowable torsion angle of the micromirror. Therefore, the pull-in torsional angle $\Theta_{\mathrm{PI}}$of the micromirror can be derived from Eq. (21) as:

$$\frac{\partial V_{\mathrm{e}}(\Theta_{\mathrm{PI}})}{\partial\Theta_{\mathrm{PI}}}=0.\tag{23}$$

Equation (23) is a partial differential equation to be solved. The traditional numerical methods are based on the mesh discretization mostly such as the finite element method and the finite difference method. Recently, neural networks [37-40] have become promising alternatives to the solution of partial differential equations due to the flexibility to define their structure and important progress in the architecture, as well as the efficiency of the algorithms to realize them. However, it is a little complex to solve the problems via the approaches above. Here the partial differential equation is solved by using intrinsic functions in MATLAB. Then, the pull-in instability voltage $V_{\mathrm{e}}^{\mathrm{PI}}$ is obtained from Eqs. (21) and (23).

Figure 3 shows the schematic diagram of the circular plate rotating along the inner axis, along the outer axis, and along the oblique axis under the action of the electrostatic force in different areas. The oblique axis rotation is that the electrostatic force in two areas acts at the same time, and their sizes can be adjusted according to needs. As shown in Fig. 3, the deflection of the circular plate in any direction in the plane can be realized by adjusting the electrostatic force region, so as to achieve the goal of deflecting the light in any direction of the micromirror and improving the flexibility of the micromirror. Equations (20) and (21) are the equations of motion rotating along the inner axis. Similarly, we can derive the following dynamic equations (24) and (25) along the outer axis and Eqs. (26) and (27) along the oblique axis:

$$I_q\frac{\partial^2\theta}{\partial t^2}+(C_{vq}+C_{sq})\frac{\partial\theta}{\partial t}+2M_{\mathrm{elas3}}+4M_{\mathrm{elas4}}-M_{\mathrm{elec}}-(1-n)\cdot M_{\mathrm{vdW}}-n\cdot M_{CT}=0,\tag{24}$$

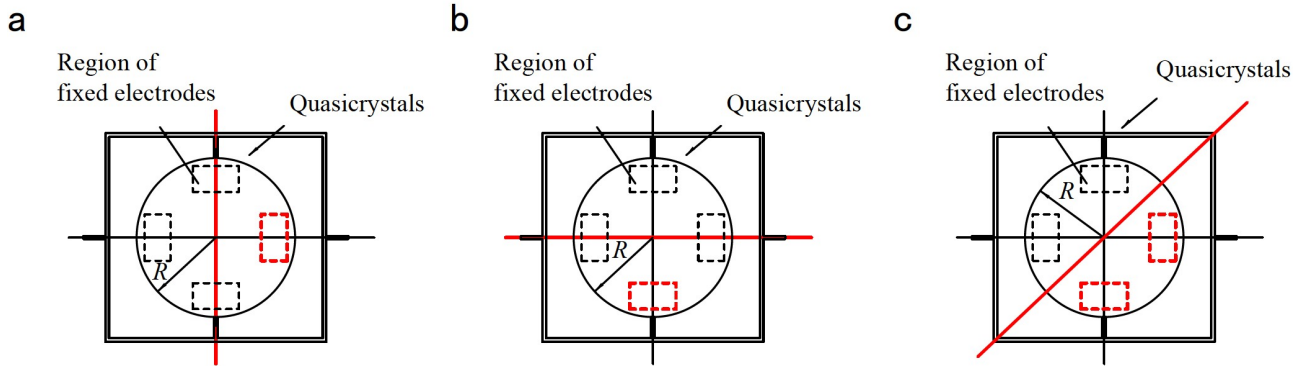

Figure 3 A schematic view of the circular plate rotating along **a** the inner axis, **b** the outer axis, and **c** the oblique axis under the action of the electrostatic force in different areas.

$$\frac{\partial^2\Theta}{\partial\tau^2}+\left[\overline{C}_{vq}+\overline{C}_{sq}\left(\frac{4}{3}+\frac{16}{5}\Theta^2+\frac{32}{7}\Theta^4\right)\right]\frac{\partial\Theta}{\partial\tau}+GJ_0\left(1+\frac{J_S}{J_0}\right)\frac{g_0(4L_3+L_2)}{2aL_2L_3}\Theta-\frac{(\varepsilon_0+\varepsilon_1)V_e^2ba^2}{2g_0^2}\frac{1}{\Theta^2}\cdot$$
$$\left[\frac{1-\Delta_2}{1-\Delta_2-\lambda_2\cdot\Theta}-\frac{1-\Delta_2}{1-\Delta_2-\lambda_1\cdot\Theta}+\ln\left(\frac{1-\Delta_2-\lambda_2\cdot\Theta}{1-\Delta_2-\lambda_1\cdot\Theta}\right)\right]-(1-n)\alpha_{3tt}\left[\frac{2(1-\Delta_2-\Theta^2)^{3/2}+3\Theta^2-2}{(1-\Delta_2-\Theta^2)^{3/2}}\right]$$
$$-\frac{n\alpha_{4tt}\Theta}{\left(1-\Delta_2-\Theta^2\right)^{5/2}}-\frac{n\alpha_{5tt}}{\Theta^3}\left[-\frac{2}{(1-\Delta_2-\Theta)^{1/2}}+\frac{\Theta^2}{(1-\Delta_2+\Theta)^{3/2}}+2\right]=0, \tag{25}$$

and

$$I_q\frac{\partial^2\theta}{\partial t^2}+(C_{\mathrm{vq}}+C_{\mathrm{sq}})\frac{\partial\theta}{\partial t}+2M_{\mathrm{elas5}}+2M_{\mathrm{elas6}}+4M_{\mathrm{elas7}}-\overline{M}_{\mathrm{elec}}-(1-n)\cdot M_{\mathrm{vdW}}-n\cdot M_{\mathrm{CT}}=0, \tag{26}$$

$$\frac{\partial^2\Theta}{\partial\tau^2}+\left[\overline{C}_{\mathrm{vq}}+\overline{C}_{\mathrm{sq}}\left(\frac{4}{3}+\frac{16}{5}\Theta^2+\frac{32}{7}\Theta^4\right)\right]\frac{\partial\Theta}{\partial\tau}+\frac{\sqrt{2}}{4}GJ_0\left(1+\frac{J_S}{J_0}\right)\frac{g_0(4L_2L_3+8L_1L_3+L_1L_2)}{aL_1L_2L_3}\Theta$$
$$-\frac{(\varepsilon_0+\varepsilon_1)V_e^2ba^2}{g_0^2\Theta^2}-(1-n)\alpha_{3tt}\left[\frac{2(1-\Delta_3-\Theta^2)^{3/2}+3\Theta^2-2}{(1-\Delta_3-\Theta^2)^{3/2}}\right]$$
$$-\frac{n\alpha_{4tt}\Theta}{\left(1-\Delta_3-\Theta^2\right)^{5/2}}-\frac{n\alpha_{5tt}}{\Theta^3}\left[-\frac{2}{(1-\Delta_3-\Theta)^{1/2}}+\frac{\Theta^2}{(1-\Delta_3+\Theta)^{3/2}}+2\right]=0, \tag{27}$$

where M_{elas3}, M_{elas4}, M_{elas5}, M_{elas6}, and M_{elas7} denote the total torques causing the torsional deformation of the rectangular section nanobeam. Δ_2 and Δ_3 are the static bending deformation of the plate rotating along the outer and oblique axes respectively. To calculate the displacement and torsion angle of the micromirror, the simultaneous equations (25) and (27) can be solved, respectively. When the pull-in torsion angle is determined by the equation, similarly, the corresponding voltage is determined in the equation.

4. Numerical examples

4.1 Validation of the proposed model with simulations

After the theoretical derivation, the instability of the model is investigated in this section. The geometric and material constants are shown in Table 1 [10]. Using MATLAB, the tilting angle, the related voltage, and velocity of rotation for instability of the micromirror system are calculated. A useful sensitivity analysis toolbox composed of a set of MATLAB functions for uncertainty analysis was provided by Vu-Bac et al. [41]. The programming skills about input parameters for the uncertainty analysis in the MATLAB code [41] are chosen as the reference of our code in the numerical calculations. To validate the results, the proposed model is compared with the finite element simulation (FES) results. The reference results are obtained by constructing a three-dimensional (3D) finite element model in ABAQUS, which is referred to as the 3D solid FES model. In this model, the material properties are the same as those in the examples of the analytical solution, and the 8-node brick element C3D8R is used for the structure. The static analysis of the solution is performed by a load-displacement algorithm (GENERAL) in ABAQUS. Figure 4 shows the stresses and displacement of the macro reference model analyzed by FES. The simulation results of three axial deflections show that the deflection along the oblique axis is the largest, the deflection along the inner axis is the second, and the deflection along the outer axis is the smallest.

Table 1 Geometrical and material parameters of the combination structure of beam and plate

Geometrical parameters	QC material parameters
H = 20 μm, R = 200 μm, a = 200 μm, $b = a/2$, $g_0 = H$, $a_1 = a$, $a_1 = 3a/2$, $L = b/2$, $L_1 = b/2$, $L_2 = 1.2R$, $L_3 = L_1$, h_1 = 10 μm, $h_2 = h_1$	$E = 197.5 \times 10^9$ N/m^2, $K_1 = 122 \times 10^9$ N/m^2, $R_1 = 17.7 \times 10^9$ N/m^2, v = 0.25

Figure 5 presents the results of the present model and the FES results. The variation of tilting angle versus voltage is plotted in Fig. 5a that increasing in applied voltage increases the tilting angle of the micromirror until the pull-in instability occurs in pull-in voltage and torsion angle finally. As shown, there is a significant difference between the torsion models with different directions of deflection axis (the inner, outer, and oblique axes) that increasing voltage to pull-in instability conditions, the difference increases continually. Therefore as mentioned previously, it should be applied with more proper electrostatic distribution to obtain the required deflection direction and get more accurate responses. The variation of maximum displacement versus voltage is plotted

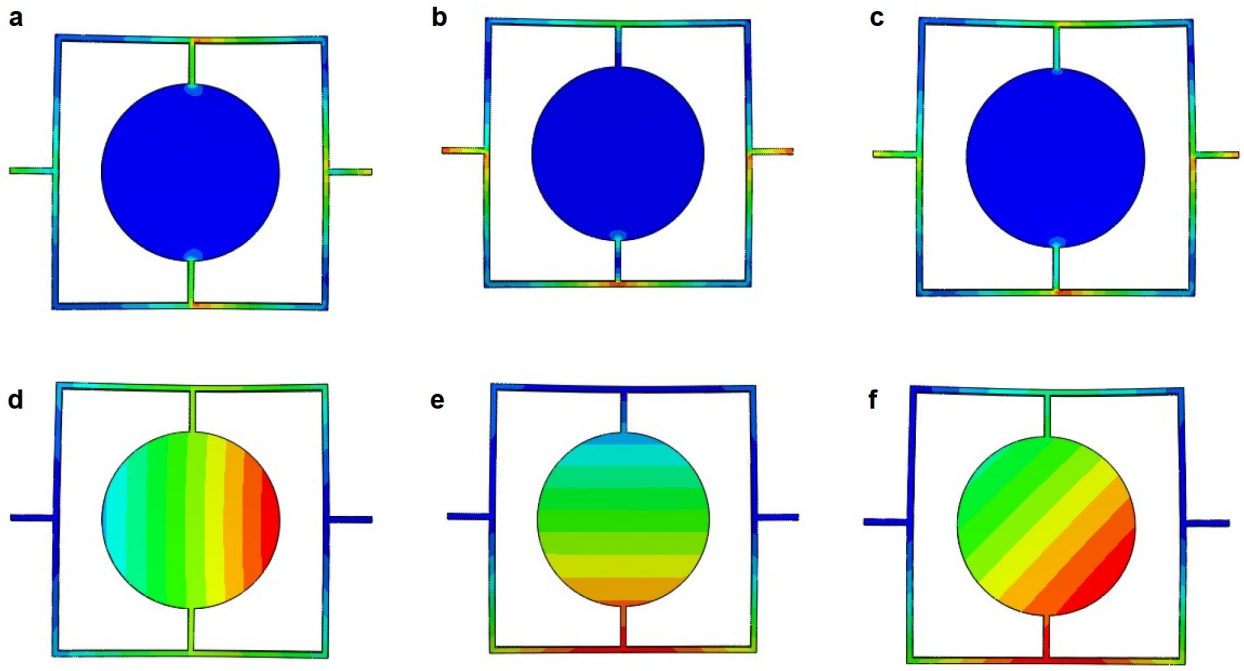

Figure 4 The static behaviors of macro reference model analyzed by finite element simulation: stress amplitude for rotating along **a** the inner axis, **b** the outer axis, and **c** the oblique axis; displacement amplitude for rotating along **d** the inner axis, **e** the outer axis, and **f** the oblique axis.

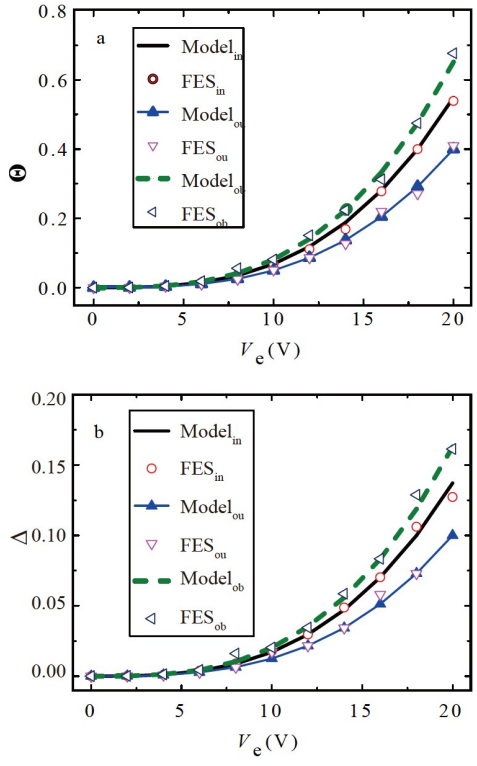

Figure 5 Comparison of torsions in three directions (the inner, outer, and oblique axes) using FES and present model for macro mirror: **a** curve for torsion angle Θ; **b** curve for maximum displacement Δ.

in Fig. 5b. According to this figure, increasing applied voltage causes an increasing displacement of the system. Like tilting angle, this increase continues until pull-in instability occurs in pull-in voltage and displacement. Based on Fig. 5, obtained results from the present model are highly close to FES results. Therefore proposed model can predict pull-in angle, displacement, and voltage in pull-in conditions with very good accuracy. In addition, compared with the mechanical behavior of Al-based nano QC materials in the previous literature [26], it is found that the numerical results of this model are in line with the reality, that is, the obtained displacements in results are feasible from a qualitative point of view.

4.2 Dynamic response of the system

In this section, different influences on the dynamic response of electrostatic torsional micromirror are investigated. Figures 6a, b show the effect of elastic moduli on the relationship between the dimensionless torsion angle and applied voltage of the micromirror system. It should be pointed out that the lower half of the relationship curve between torsion angle and applied voltage reflects the actual pull-in instability process, while the upper half satisfies the micromirror equilibrium equation, but it has no physical significance. As shown in Fig. 6, the pull-in instability voltage increases with the increase of phonon-phason coupling elastic modulus and phason elastic modulus. However, the position of the pull-in buckling torsional angle $\Theta = 0.5$ does not change significantly. This shows that the smaller elastic constants in the phason field make the micromirror more prone to instability. Figures 6c, d compare the curves of

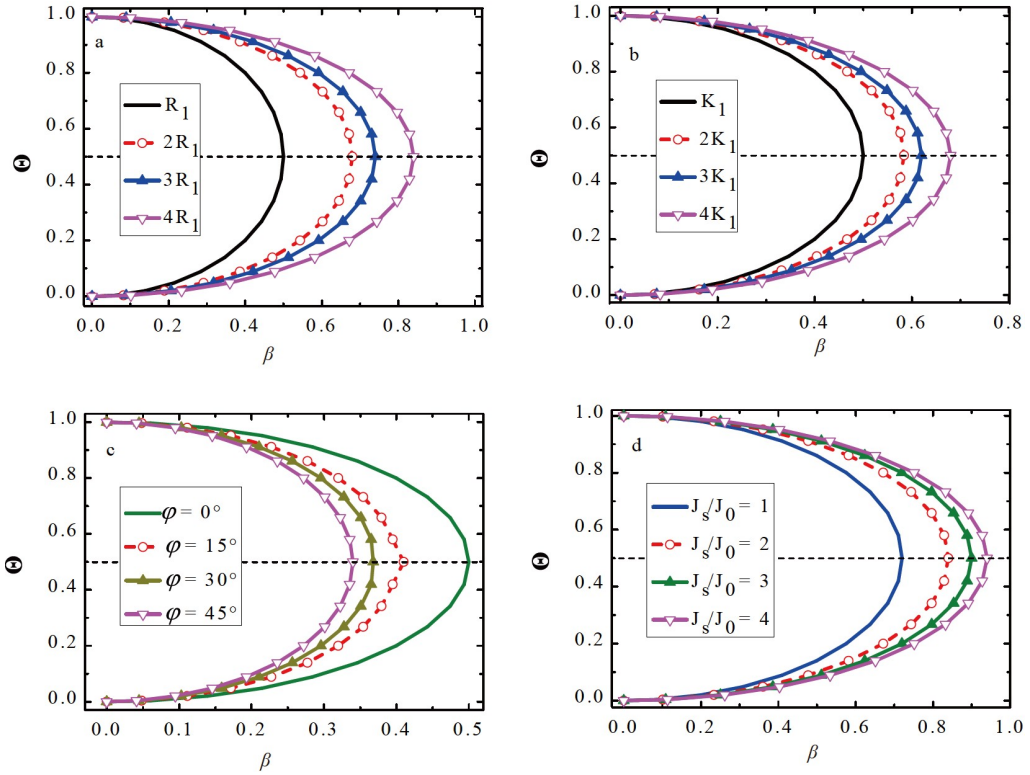

Figure 6 Influences of **a** phonon-phason coupling elastic modulus R_1 and **b** phason elastic modulus K_1, and influences of **c** horizontal deflection angle φ and **d** strain gradient parameter-induced additional stiffness J_s/J_0 on the dimensionless pull-in tilting angle Θ and voltage β, respectively.

torsion angle versus applied voltage under different deflection directions and ratios of width to thickness of the beam. When the deflection angle reaches 45°, as it deflects along the inclined 45° axis, the pull-in voltage is the minimum. This shows that the deflection in the oblique direction makes the micromirror more prone to instability. The dimensionless pull-in tilting angle and voltage reach the minimum when the strain gradient parameter-induced additional stiffness J_s/J_0 equals one in Fig. 6d. This means that with the increase of the torsional stiffness ratio, the pull-in instability voltage of QC micromirror increases.

Dimensionless variations of tilting angle Θ and velocity of rotation ξ versus dimensionless time τ are plotted in Fig. 7. It is evident from these figures that the system has oscillatory motion at a voltage less than the pull-in voltage and will eventually approach a specified quantity with the presence of the extruded air damping so that in this case the torsion angle will approach a non-zero quantity and the rotation speed will approach a zero quantity. If the applied voltage increases slightly, the system will have voltage instability because the voltage is greater than the pull voltage. During this time, the system becomes non-oscillating and tends to be infinite.

Variations of normalized tilting angle versus dimensionless time with different strain gradient parameter-induced additional stiffness are illustrated in Fig. 7a. It is observed that the oscillation becomes more severe when strain gra-

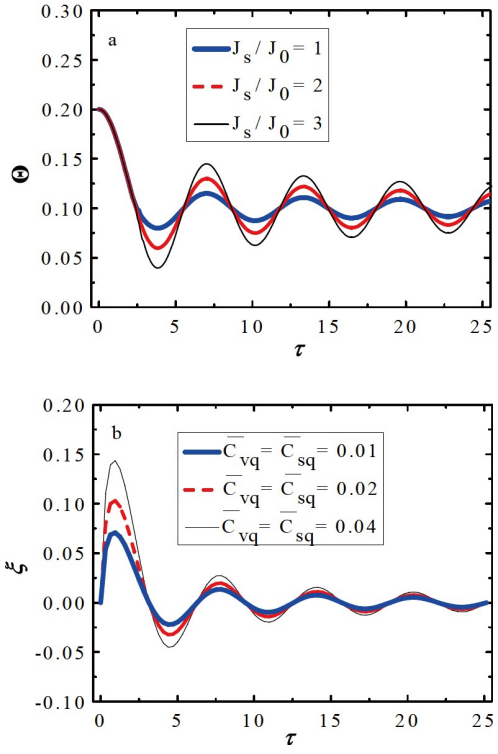

Figure 7 Comparison of time history curves of **a** the tilting angle Θ with different strain gradient parameter-induced additional stiffness J_s/J_0 and **b** the velocity of rotation ξ with different damping effects $\overline{C}_{vq}$ and $\overline{C}_{sq}$, respectively.

dient parameter-induced additional stiffness increases, indicating that the strain gradient parameters have a significant effect on the deflection process. Moreover, with the variation of the magnitude of the torsion angle, the position of stable and unstable equilibrium points is changed through the size effect caused by the strain gradient parameter. This effect decreases the stable equilibrium point and increases the unstable equilibrium point of the system. So the importance of considering size effect on analyzing micromirror behavior appears exactly. Figure 7b shows the effect of damping dissipation $\overline{C}_{vq}$ and $\overline{C}_{sq}$on the curve of torsional velocity versus time of the micromirror dynamic system. The results show that when the damping effect is considered, the torsional speed of the micromirror decreases with time. Due to the constant loss of energy of the micromirror system, if there is no new electric energy compensation, the dynamic system will eventually stop moving. When the damping coefficient is increased, the attenuation of torsional velocity is accelerated, and the energy dissipation of the micromirror system is also more significant so that the system stops moving in a shorter time. This indicates that the existence of air damping accelerates the energy dissipation of the micromirror system, and has a significant influence on the torsional velocity and torsional angle amplitude.

Figure 8 shows the effect of QC permittivity on the maximum torsional angle Θ_m of the micromirror system during the movement in Fig. 7. As can be seen from Fig. 8, the effect of capacitance caused by the epilayer of QC surface significantly increases the value of torsion angle of the micromirror, which can be reflected in Eq. (1). Figure 8a also shows the effect of the damping coefficient on the torsional angle. The maximum torsional angle decreases with the increment of the coefficient, which reflects the blocking effect of air damping on the motion. In addition, the influence of parameters λ of the fixed electrode position and width on the torsion angle is shown in Fig. 8b. The results show that the torsion angle decreases with the increasing parameters. With the increase of the parameters, the closer the electrode position is to the rotation axis, the smaller the deflection bending moment.

Figure 9 compares the influence of the damping effect on the planar phase diagram characteristics of the micromirror system when the applied voltage is 0.5 and the plate spacing is still greater than the pull-in instability displacement. According to the results of Fig. 9a without considering the influence of damping effect, when the applied voltage has not reached the pull-in instability voltage and the plate spacing is greater than the pull-in instability displacement, there are two equilibrium points in the micromirror dynamic system, one is a stable center P and the other is an unstable saddle point Q; there are periodic orbits around the stable center P, and homoclinic orbits originate and terminate at the saddle

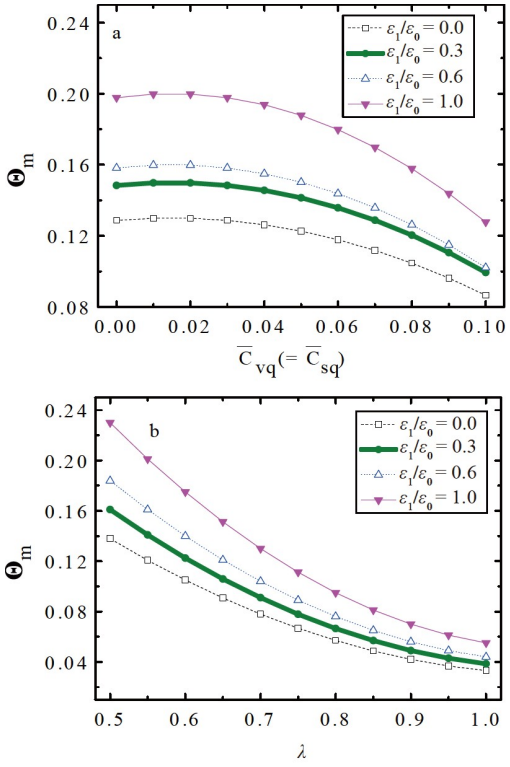

Figure 8 Influence of QC permittivity ε_1 on the maximum torsion angle Θ_m with different **a** damping effects $\overline{C}_{vq}(=\overline{C}_{sq})$ and **b** parameters of outer electrode position and width $\lambda = b/a_1$.

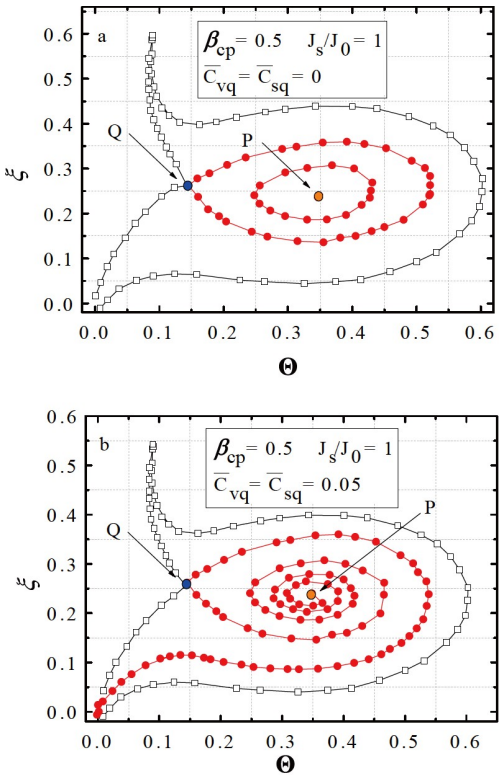

Figure 9 Comparison of the phase portrait on the phase plane: **a** without damping effects ($\overline{C}_{vq} = \overline{C}_{sq} = 0$) and **b** with damping effects ($\overline{C}_{vq} = \overline{C}_{sq} = 0.05$).

point Q. When the damping effect is considered, the micromirror dynamic system still has two equilibrium points but becomes a stable focus P and an unstable saddle point Q. There are asymptotically spiral orbits around the stable focus P, and the heteroclinic orbits of the system diverge after passing through the saddle point Q due to the damping dissipation. It can be seen that the damping effect obviously changes the basic characteristics of the planar phase diagram of the micromirror system, and has an important impact on the stability of the dynamic system.

The surface forces distributed on the bottom surface of the circular plate include electrostatic, van der Waals, and Casimir forces. The influences of van der Waals moment and thermal Casimir moment on the pull-in instability voltage are shown in Fig. 10a, b, where α_3 and α_4 represent the coefficients in front of the expressions of van der Waals and Casimir forces, respectively. With the increase of micro-distribution moment, the pull-in instability voltage of micromirror decreases, and the influence of thermal Casimir moment on the pull-in instability parameters is more obvious. In addition, the micromirror instability occurs later with the increase of the initial gap in Fig. 10, which corresponds to the larger electrostatic load. This shows that the pull-in instability of the QC plate is affected by the micro-distributed forces on the surface.

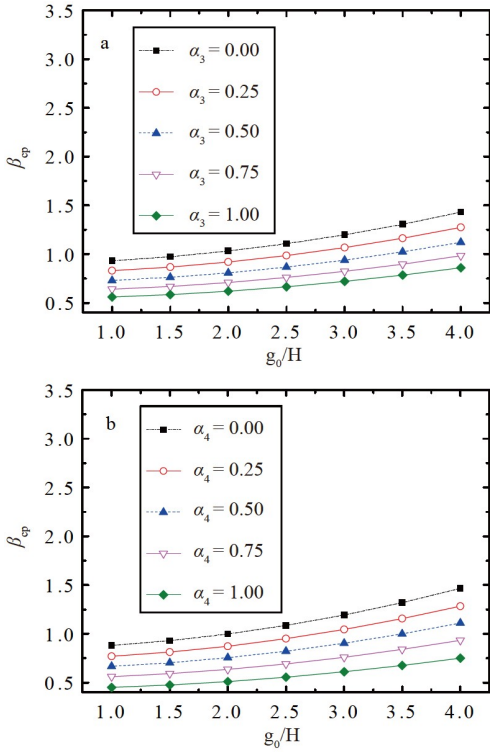

Figure 10 Influence of **a** van der Waals moment ($\alpha_3 = 0$) and **b** thermal Casimir moment ($\alpha_4 = 0$) on the pull-in voltage β_{cp} with different initial gap g_0.

5. Conclusions

Dynamic response and stability of electrostatic QC torsional micromirror under distributed forces and squeeze film air damping considering size effect in strain gradient theory are studied in this paper. A micromirror system model of rectangular mainboard considering the torsion bending coupling deformation of the beam is established, and the effects of structural parameters on the pull-in instability torsion angle, displacement, and voltage are analyzed. The following results are achieved:

(1) There are significant differences in torsion models with different deflection axis directions. Therefore, appropriate electrostatic distribution should be used to obtain the required deflection direction and more accurate responses. When the deflection angle along the oblique axis reaches 45°, the instability voltage is the smallest and the deflection is the largest.

(2) The pull-in instability voltage increases with the increase of phonon-phason coupling elastic modulus and phason elastic modulus. Also, the pull-in instability voltage becomes larger with the increase of the initial gap and the decrease of surface distributed forces.

(3) The permittivity of quasicrystal and the strain gradient parameter have significant effects on the deflection process. The damping effect also affects the torsional speed of the micromirror dynamic system. When the damping coefficient increases, the attenuation of torsional velocity is accelerated, which makes the system stop moving in a short time.

The work was supported by the National Natural Science Foundation of China (Grant Nos. 11572191, 51701117, and 51779139).

1 M. E. Motamedi, MOEMS: Micro-Opto-Electro-Mechanical Systems (SPIE Press, Bellingham, 2005).
2 W. Sun, J. Lan, and J. T. W. Yeow, Constraint adaptive output regulation of output feedback systems with application to electrostatic torsional micromirror, Int. J. Robust Nonlin. Control **25**, 504 (2015).
3 M. Taghizadeh, and H. Mobki, Bifurcation analysis of torsional micromirror actuated by electrostatic forces. Arch. Mech. **66**, 95 (2014).
4 C. S. Harsha, C. S. Prasanth, and B. Pratiher, Prediction of pull-in phenomena and structural stability analysis of an electrostatically actuated microswitch, Acta Mech. **227**, 2577 (2016).
5 X. M. Zhang, F. S. Chau, C. Quan, Y. L. Lam, and A. Q. Liu, A study of the static characteristics of a torsional micromirror, Sens. Actuat. A-Phys. **90**, 73 (2001).
6 D. Sadhukhan, and G. P. Singh, Study of Electrostatic Actuated MEMS Biaxial Scanning Micro-Mirror with Comb Structure. Inter. Confer. Multi. Mater. 2019, doi: 10.1063/5.0019578.
7 Y. Hua, S. Wang, B. Li, G. Bai, and P. Zhang, Dynamic modeling and anti-disturbing control of an electromagnetic mems torsional micromirror considering external vibrations in vehicular LiDAR, Micromachines **12**, 69 (2021).
8 W. M. Zhang, H. Yan, Z. K. Peng, and G. Meng, Electrostatic pull-in instability in MEMS/NEMS: A review, Sens. Actuat. A-Phys. **214**, 187 (2014).
9 F. Khatami, and G. Rezazadeh, Dynamic response of a torsional micromirror to electrostatic force and mechanical shock, Microsyst. Technol. **15**, 535 (2009).

10 Q. Li, J. Xi, and C. Hua, Bifurcations of a micro-electromechanical nonlinear coupling system, Commun. Nonlin. Sci. Numer. Simul. **16**, 769 (2011).
11 S. Malihi, Y. T. Beni, and H. Golestanian, Dynamic pull-in stability of torsional nano/micromirrors with size-dependency, squeeze film damping and van der waals effect, Optik **128**, 156 (2017).
12 F. M. M. Seyyed, A. Rastgoo, and M. Taghi Ahmadian, Size-dependent instability of carbon nanotubes under electrostatic actuation using nonlocal elasticity, Int. J. Mech. Sci. **80**, 144 (2014).
13 H. Ren, X. Zhuang, and T. Rabczuk, A nonlocal operator method for solving partial differential equations, Comput. Methods Appl. Mech. Eng. **358**, 112621 (2020).
14 H. Ren, X. Zhuang, and T. Rabczuk, A higher order nonlocal operator method for solving partial differential equations, Comput. Methods Appl. Mech. Eng. **367**, 113132 (2020).
15 M. Shaat, F. F. Mahmoud, X. L. Gao, and A. F. Faheem, Size-dependent bending analysis of Kirchhoff nano-plates based on a modified couple-stress theory including surface effects, Int. J. Mech. Sci. **79**, 31 (2014).
16 H. M. Sedighi, Size-dependent dynamic pull-in instability of vibrating electrically actuated microbeams based on the strain gradient elasticity theory, Acta Astronaut. **95**, 111 (2014).
17 K. F. Wang, and B. L. Wang, A general model for nano-cantilever switches with consideration of surface effects and nonlinear curvature, Phys. E-Low-dimen. Syst. Nanostruct. **66**, 197 (2015).
18 A. Zabihi, R. Ansari, J. Torabi, F. Samadani, and K. Hosseini, An analytical treatment for pull-in instability of circular nanoplates based on the nonlocal strain gradient theory with clamped boundary condition, Mater. Res. Express **6**, 0950b3 (2019).
19 A. A. Daikh, M. S. A. Houari, and A. Tounsi, Corrigendum: Buckling analysis of porous FGM sandwich nanoplates due to heat conduction via nonlocal strain gradient theory (2019 Eng. Res. Express 1 015022), Eng. Res. Express **2**, 049501 (2020).
20 A. Zabihi, J. Torabi, and R. Ansari, Effects of geometric nonlinearity on the pull-in instability of circular microplates based on modified strain gradient theory, Phys. Scr. **95**, 115204 (2020).
21 S. M. J. Hosseini, J. Torabi, R. Ansari, and A. Zabihi, Geometrically nonlinear electromechanical instability of fg nanobeams by nonlocal strain gradient theory, Int. J. Str. Stab. Dyn. **21**, 2150051 (2021).
22 B. Hu, J. Liu, Y. Wang, B. Zhang, and H. Shen, Wave propagation in graphene reinforced piezoelectric sandwich nanoplates via high-order nonlocal strain gradient theory, Acta Mech. Sin. doi: 10.1007/s10409-021-01113-y (2021).
23 S. M. J. Hosseini, R. Ansari, J. Torabi, K. Hosseini, and A. Zabihi, Nonlocal strain gradient pull-in study of nanobeams considering various boundary conditions, Iran J. Sci. Technol. Trans. Mech. Eng. **45**, 891 (2021).
24 J. M. Dubois, Useful Quasicrystals (World Scientific, Singapore, 2005).
25 T. Y. Fan, The Mathematical Theory Elasticity of Quasicrystals and its Applications (Springer, Singapore, 2010).
26 V. Fournée, H. R. Sharma, M. Shimoda, A. P. Tsai, B. Unal, A. R. Ross, T. A. Lograsso, and P. A. Thiel, Quantum size effects in metal thin films grown on quasicrystalline substrates, Phys. Rev. Lett. **95**, 155504 (2005).
27 A. Inoue, F. Kong, S. Zhu, C. T. Liu, and F. Al-Marzouki, Development and applications of highly functional Al-based materials by use of metastable phases, Mat. Res. **18**, 1414 (2015).
28 L. Zhang, J. Guo, and Y. Xing, Bending analysis of functionally graded one-dimensional hexagonal piezoelectric quasicrystal multilayered simply supported nanoplates based on nonlocal strain gradient theory, Acta Mech. Solid Sin. **34**, 237 (2021).
29 X. Li, J. Guo, and T. Sun, Bending deformation of multilayered one-dimensional quasicrystal nanoplates based on the modified couple stress theory, Acta Mech. Solid Sin. **32**, 785 (2019).
30 S. Malihi, Y. T. Beni, and H. Golestanian, Analytical modeling of dynamic pull-in instability behavior of torsional nano/micromirrors under the effect of Casimir force, Optik **127**, 4426 (2016).
31 P. A. Thiel, Quasicrystal surfaces, Annu. Rev. Phys. Chem. **59**, 129 (2008).
32 I. Brevik, J. B. Aarseth, J. S. Høye, and K. A. Milton, Temperature dependence of the Casimir effect, Phys. Rev. E **71**, 056101 (2005).
33 F. Pan, J. Kubby, E. Peeters, A. T. Tran, and S. Mukherjee, Squeeze film damping effect on the dynamic response of a mems torsion mirror, J. Micromech. Microeng. **8**, 200 (1999).
34 R. Atabak, H. M. Sedighi, A. Reza, and E. Mirshekari, Analytical investigation of air squeeze film damping for bi-axial micro-scanner using eigenfunction expansion method, Math. Meth. Appl. Sci. mma.6658 (2020).
35 J. Abdi, M. Keivani, and M. Abadyan, Microstructure-dependent dynamic stability analysis of torsional NEMS scanner in van der Waals regime, Int. J. Mod. Phys. B **30**, 1650109 (2016).
36 P. Tong, F. Yang, D. C. C. Lam, and J. Wang, Size effects of hair-sized structures-torsion, Key Eng. Mater. **261-263**, 11 (2004).
37 E. Samaniego, C. Anitescu, S. Goswami, V. M. Nguyen-Thanh, H. Guo, K. Hamdia, X. Zhuang, and T. Rabczuk, An energy approach to the solution of partial differential equations in computational mechanics via machine learning: Concepts, implementation and applications, Comput. Methods Appl. Mech. Eng. **362**, 112790 (2019).
38 C. Anitescu, E. Atroshchenko, N. Alajlan, and T. Rabczuk, Artificial neural network methods for the solution of second order boundary value problems, Comput. Mater. Continua **59**, 345 (2019).
39 H. Guo, X. Zhuang, and T. Rabczuk, A deep collocation method for the bending analysis of Kirchhoff plate, Comput. Mater. Continua **59**, 433 (2019).
40 T. Rabczuk, H. Ren, and X. Zhuang, A nonlocal operator method for partial differential equations with application to electromagnetic waveguide problem, Comput. Mater. Continua **59**, 31 (2019).
41 N. Vu-Bac, T. Lahmer, X. Zhuang, T. Nguyen-Thoi, and T. Rabczuk, A software framework for probabilistic sensitivity analysis for computationally expensive models, Adv. Eng. Software **100**, 19 (2016).

基于应变梯度理论的准晶扭转微镜驱动器的稳定性分析

黄允祇, 冯淼林, 陈秀华

摘要 静电扭转微镜广泛应用于微米光开关、光衰减器、光学扫描仪和光学显示器等领域. 过去微镜镜面主要沿单轴或双轴方向偏转, 从而限制了入镜光线的反射范围. 本文通过建立圆形静电驱动微镜的动力学模型, 设计了一种可任意方向偏转的准晶微镜驱动器. 然后基于应变梯度理论进行数值求解, 分析了其静态和动态现象以及吸合失稳特性, 并比较了反射镜面在三种偏转方向下的结果. 研究表明, 镜面沿着不同方向偏转的结果存在显著差异. 当沿斜轴的偏转角度达到45°时, 吸合失稳电压值最小. 失稳电压还随着准晶的声子场-相位子场耦合弹性模量和相位子场弹性模量的增加而增加. 准晶的介电常数、应变梯度参数和空气阻尼都会影响到微镜动态系统的扭转. 此外, 微镜表面分布力的减小也会导致更大的吸合失稳电压.